Operation and Design Consideration of an Ultrahigh Step-Up DC–DC Converter Featuring High Power Density

Hadi Tarzamni, *Student Member, IEEE*, Mehran Sabahi, Saeed Rahimpour, Matti Lehtonen, *Member, IEEE*, and Payman Dehghanian, *Senior Member, IEEE*

***Abstract*— A new dual-coupled inductor (CI) single-switch high step-up dc–dc topology featuring high power density is proposed in this study. Various capacitive power transfer methods, as well as inductive power transfer techniques, are utilized to act as a more efficient power interface between the input and the load. Three ports in the output terminal are employed to distribute the overall output voltage, diminish the voltage ripple in high-voltage gain ratios, and decrease the voltage stress on the port component. In the proposed converter, first, the voltage gain is high in lower duty cycles of the switching. Second, the stored energy of magnetizing and leakage inductances is recycled in both Cls. Third, the switch voltage spikes are alleviated. Fourth, the operation is done with no circulating current. Fifth, low-size passive components are presented. Sixth, high power density is obtained, and the voltage range is widened. Finally, a simple pulsewidth modulation (PWM) utilizing a wide control range is provided. In this study, the steady-state operation is analyzed under both continuous conduction mode (CCM) and discontinuous conduction mode (DCM), and the performance of the converter is evaluated using comparisons with similar works. In addition, the experimental results have been provided to justify the feasibility of the design.**

***Index Terms*— Coupled inductor (CI), dc–dc power conversion, high power density, high step-up converter.**

I. Introduction

THE design of dc–dc converters is typically challenging [1]–[3], where increasing the voltage gain and achieving a higher level of output voltage is always a key concern [4]–[6]. There are some typical approaches that can be utilized to boost the voltage gain, including switched-capacitor (SC) modules, coupled inductors (CIs), and voltage multiplier cells (VMCs). If no inductors are used in the converter structure, SC converters distribute the voltage stress of the main switch and the capability of the resulting converter in voltage boosting is extendable. Nevertheless, the drawbacks of such converters with low efficiency are the inrush currents of the capacitors during switching transitions, balancing difficulty in the voltage of the capacitors, considerable switching losses, and high current stress over the main switch [7]. In addition, the components suffer from considerably high *di/dt* during their switching transitions. Thus, this issue should be resolved by applying an auxiliary current snubber [8]. Therefore, CIs are still attractive candidates in achieving high-voltage gain feature in the dc–dc converters.

Embedding CIs in the converters can be beneficial in increasing the voltage gain, even by setting medium turns ratio of the CI or a medium range of the duty cycle. Doing so will alleviate the issues of reverse recovery on rectifier diodes. In [9] and [10], two similar converters with a single switch and featuring high step-up voltage gain have been presented. These converters combined CI and VMC as an effort to improve voltage gain with recycling the energy in the leakage inductance. The main drawbacks of these converter structures are considerably high inrush current of VMC (within the switching transition time) and higher ripples in the output voltage. Using the same approach, the scholars in [11] utilized two switches in order to achieve a soft-switching performance of the converter. Even though the focus in [11] is on reducing the switching loss, using two switches in the structure leads to the increase in the conduction loss, which makes the control of the switches more arduous, and the range of the duty cycle in the main switch will be narrowed. The interleaving method has been utilized in [12] in a coupled-inductor-based converter. The presented structure draws current in the input with low ripple, and the voltage stress on the switch has been decreased. On the other hand, the number of semiconductor elements is considerable, where their parasitic capacitances play an important role to ensure faultless operation. The scholars in [13] have combined VMC and CI and employed them in an interleaved boost converter as an effort to improve the voltage gain in the output terminal of the converter. Nevertheless, the size of the converter is increased due to the use of two large CIs.

Two dc–dc converters with similar structures have been suggested in [14] and [15], which employ VMC and CI

Manuscript received August 27, 2020; revised December 6, 2020 and February 12, 2021; accepted April 5, 2021. Date of publication April 13, 2021; date of current version October 1, 2021. Recommended for publication by Associate Editor Xinbo Ruan. *(Corresponding author: Mehran Sabahi.)*

Hadi Tarzamni and Matti Lehtonen are with the Department of Electrical Engineering and Automation, Aalto University, 02150 Espoo, Finland (e-mail: hadi.tarzamni@aalto.fi; matti.lehtonen@aalto.fi).

Mehran Sabahi is with the Faculty of Electrical and Computer Engineering, University of Tabriz, Tabriz 51666-15813, Iran (e-mail: sabahi@tabrizu.ac.ir).

Saeed Rahimpour is with the Department of Electrical Engineering, Guilan University, Rasht 4199613776, Iran (e-mail: s.rahimpour@gmail.com).

Payman Dehghanian is with the Department of Electrical and Computer Engineering, George Washington University, Washington, DC 20052 USA (e-mail: payman@gwu.edu).

Color versions of one or more figures in this article are available at https://doi.org/10.1109/JESTPE.2021.3072957.

Digital Object Identifier 10.1109/JESTPE.2021.3072957

to reduce the voltage stress while enhancing the voltage gain. However, the leakage inductance and the magnetizing inductance are not suitably applied. A three-phase interleaved converter has been proposed in [16] in order to feature high-voltage gain. The structure employs two switches, as well as a CI in each phase, making the converter bulky and expensive to implement. The dc–dc converter, which is introduced in [17], focused on achieving a high-voltage gain and soft-switching performance. The main drawback of this converter is its high input current ripple. In addition, the duty cycle that is needed for achieving the intended voltage gain is high, which yields more conduction loss. Utilizing the interleaved method, two step-up converters have been presented in [18] and [19]. These converter structures focused on autobalancing of the input current. These approaches suffer from some disadvantages, including electromagnetic interference (EMI) problem, considerable resonating currents, and excessive operational modes, which make its control more complex. CI and VMC have been incorporated in [20] to make an interleaved dc–dc converter with high-voltage gain and low input current ripple features. Nevertheless, the excessive number of the circuit elements and limited duty cycle range are the main drawbacks of this structure. In the suggested approach in [21], the scholars concentrated on reducing the ripples in the input current. The feasibility of this interleaved-CI dc–dc converter in practical implementation is limited by less efficient VMC.

The state-of-the-art CI-embedded converter topologies are mainly suffering from the following shortcomings: 1) inefficient utilization of leakage and magnetizing inductances; 2) the issue with the amount of ripples in the output voltage; 3) excessive utilization of components yielding to lower power density; 4) circulating current losses; 5) limited duty cycle region; 6) the issue with the excessive number of CI turns ratio or high duty cycle to achieve high output voltage gains; and 7) the problem with the inrush current of VMC capacitors during switching transitions. To resolve the abovementioned drawbacks, we propose a high step-up dc–dc converter that mitigates or eliminates the aforementioned limitations with wide applications in electroplating, dc power supplies, motor driving systems, and renewable energy systems such as photovoltaic. This article is presented in different sections, as operation analytics, calculations of the power loss, design procedure, comparison study, and experimental results of a 600-W prototype.

II. Proposed Converter

The proposed dc–dc converter utilizing dual-CI and featuring high step-up voltage gain is shown in Fig. 1. This converter is made up of one power switch (S), six diodes (D_1–D_6), two CIs with two and three windings, and four capacitors (C, C_{o1}, C_{o2}, and C_{o3}). The three-winding CI is modeled as an ideal transformer with turn ratios of n_1: n_2: n_3, as well as magnetizing inductance (L_m) and leakage inductances (L_{r1} and L_{r2}). The input CI is also modeled as an ideal transformer with n_4: n_5 turn ratios and inductances of L_n, L_{k1}, and L_{k2}. In the converter structure, the voltage in the input (V_i)

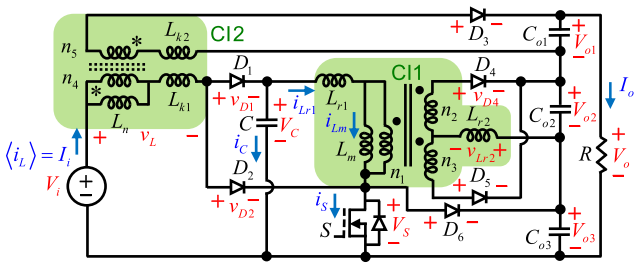

Fig. 1. Proposed structure of high step-up dc–dc converter.

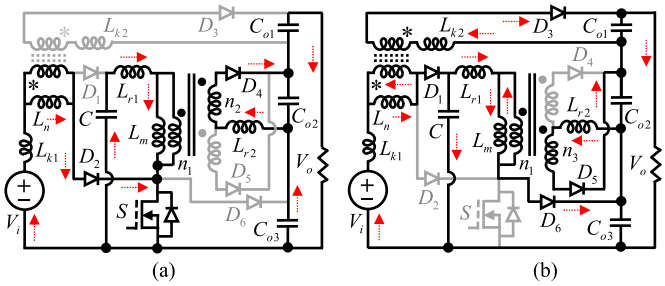

Fig. 2. Flow of current in CCM operational intervals: (a) Interval 1 and (b) Interval 2.

is converted into high output voltages (V_{o1}, V_{o2}, and V_{o3}) via flyback and forward techniques. In the output terminal, the configuration of the corresponding capacitors (C_{o1}, C_{o2}, and C_{o3}) provides the output voltage (V_o).

A. Continuous Conduction Mode Operational Intervals

Continuous conduction mode (CCM) operation of the proposed converter consists of two intervals, which are distinguished by the ON and OFF states of the S switch (see Fig. 2). The performance of the converter is investigated by assuming the following conditions.

1) The components are considered ideal.
2) The waveforms and the operational analytics are in the steady state of the converter.
3) The capacitor voltages (V_C, V_{o1}, V_{o2}, and V_{o3}) are assumed to be without any ripple.
4) In case the values of voltage and current are low in the primary (low voltage) and secondary (high voltage) sides of the CI, respectively, the regarding voltage and current of the leakage inductances (v_{Lr1} and i_{Lr2}) are neglected.

Each operational interval is explained and formulated in the following, and Fig. 3 shows the main components' waveforms in the steady state of the components assuming the abovementioned conditions. As shown in Fig. 3, the single switch of the proposed converter (S) is driven through a pulsewidth modulation (PWM) control (G_S), which results in its ON and OFF states in $0 < t < DT_S$ and $DT_S < t < T_S$, respectively.

Interval 1($0 < t < DT_S$): According to Fig. 2(a), switch S is ON and V_i charges $L = L_n + L_k$ via D_2, which yields

$$i_L(t) = \frac{V_i}{L}t + I_L(0) \tag{1}$$

where $I_L(0)$ is the initial current of L at $t = 0$.

The OFF state of D_3 blocks the transfer of the input power to V_{o1}. The stored energy in C charges L_m and is transferred

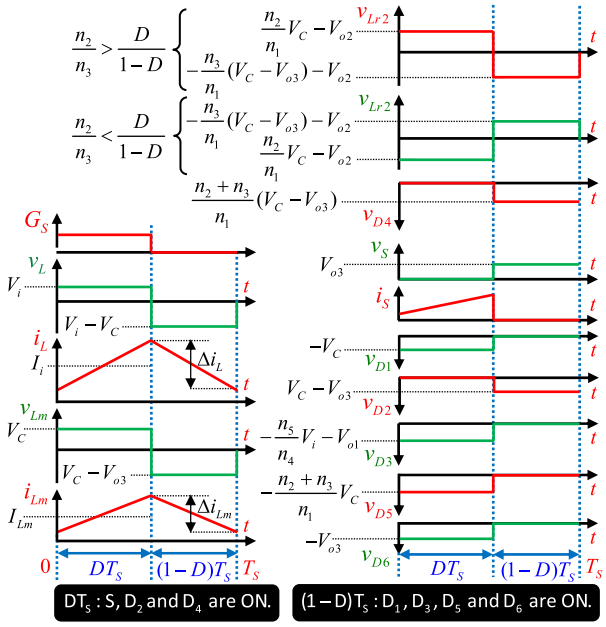

Fig. 3. Main steady-state voltage and current waveforms of CCM.

to n_2 and V_{o2} through n_1, which turns the diode D_4 ON. The voltages across L_m and L_{r2} (v_{Lm} and v_{Lr2}) are calculated as

$$v_{Lm} = \frac{V_i}{(1-D)}, \quad v_{Lr2} = V_i \frac{n_2 - D(n_2+n_3)}{n_1(1-D)} \tag{2}$$

where D represents the duty cycle of S. Thus, it can be inferred that the sign of v_{Lr2} could be either + or – according to the values of D, n_2, and n_3, which decides the charging or discharging states of L_{r2}—i.e., $di_{Lr2}/dt > 0$ or $di_{Lr2}/dt < 0$. As shown in Fig. 3, the flow of energy can also be determined in intervals 1 and 2. The following equations outline the operation:

$$\begin{cases} n_2/n_3 > D/(1-D), & L_{r2} \text{ is charged in } DT_S \\ n_2/n_3 < D/(1-D), & L_{r2} \text{ is charged in } (1-D)T_S. \end{cases} \tag{3}$$

Interval 2 ($DT_S < t < T_S$): Following the switch duty cycle, S is turned off at $t = DT_S$, which turns the switching states of diodes D_1, D_2, D_3, D_4, D_5, and D_6 into ON, OFF, ON, OFF, ON, and ON states, respectively. In the next step, the energy that was saved in the inductance (L_k) is discharged to the capacitor (C). Therefore, the energy is transferred to C_{o3}, where $i_L(t)$ is reduced according to the following equation:

$$i_L(t) = -\frac{V_i D}{L(1-D)}(t - DT_S) + \frac{V_i D}{f_S L} + I_L(0) \tag{4}$$

then, f_s indicates the switching frequency of the converter.

Furthermore, the saved energy in L_n and L_m is discharged to C_{o1} and C_{o2}, respectively, through D_3 and D_5. In case the main switch of the converter is turned off, the energy recycle of L_n and L_m in this interval is the same as the flyback converter. Thus, v_{Lm} can be obtained as follows:

$$v_{Lm} = \frac{-V_i D}{(1-D)^2}. \tag{5}$$

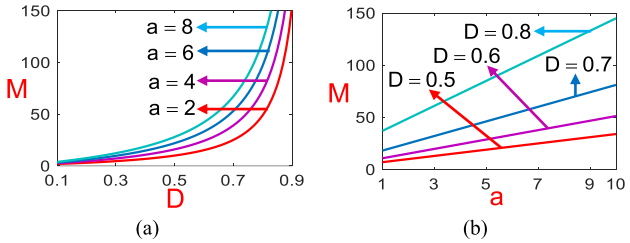

Fig. 4. Voltage gain in terms of (a) duty cycle and (b) CI turns ratio.

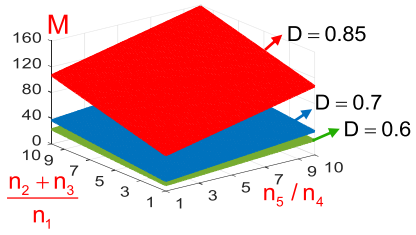

Fig. 5. Voltage gain with respect to $(n_2 + n_3)/n_1$ and n_5/n_4.

L_{r2} operates according to the mentioned condition in (3). Hence, v_{Lr2} is calculated by applying the following equation:

$$v_{Lr2} = V_i \frac{n_3 D - D(1-D)(n_2+n_3)}{n_1(1-D)^2}. \tag{6}$$

B. Voltage Gain

The voltage gain of the proposed converter is calculated by applying the volt-second balancing law (VSBL) to the inductors (L, L_m, and L_{r2}), according to the corresponding voltage values in Fig. 3 for the ON period of the switch (DT_S) and the OFF period of the switch $[(1-D)T_S]$. Hence, the voltage gain of each output terminal can be obtained as follows:

$$V_C = \frac{V_i}{(1-D)}, \quad V_{o1} = \frac{V_i D}{1-D}\left(\frac{n_5}{n_4}\right) \tag{7}$$

$$V_{o2} = \frac{V_i D}{1-D}\left(\frac{n_2+n_3}{n_1}\right), \quad V_{o3} = \frac{V_i}{(1-D)^2}. \tag{8}$$

Therefore, the output voltage gain (M) can be derived as follows:

$$M = \frac{V_{o1}+V_{o2}+V_{o3}}{V_i} = \frac{D}{1-D}\left(\frac{n_2+n_3}{n_1}+\frac{n_5}{n_4}\right) + \frac{1}{(1-D)^2}. \tag{9}$$

As assessed in (9), M depends on both D and turns ratio of the CIs with direct relation, which provides a large output voltage range. Figs. 4 and 5 show 2-D and 3-D graphical views of (9) in terms of D, a, $(n_2+n_3)/n_1$, and n_5/n_4 by assuming $a = n_2/n_1 = n_3/n_1 = n_5/n_4$.

C. Voltage Stress Analysis

Through the resulted capacitor voltage equations in (7) and (8), the voltage stress of the power switch (S) during $(1-D)T_S$ can be calculated by applying (10). As shown in Fig. 6, the

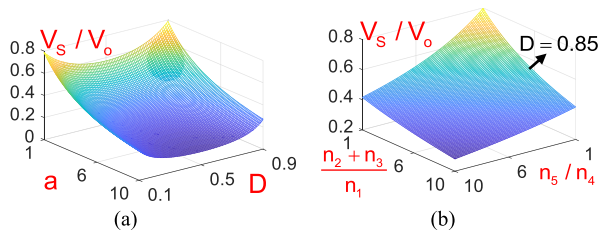

Fig. 6. Normalized switch voltage stress with respect to (a) D and a and (b) $(n_2 + n_3)/n_1$ and n_5/n_4.

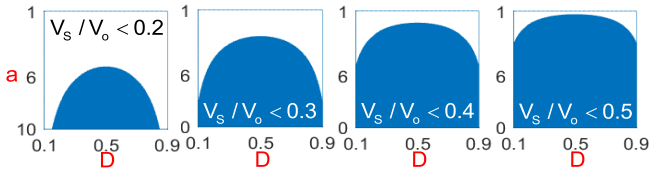

Fig. 7. Desired operation area for low switch voltage stress with respect to a and D.

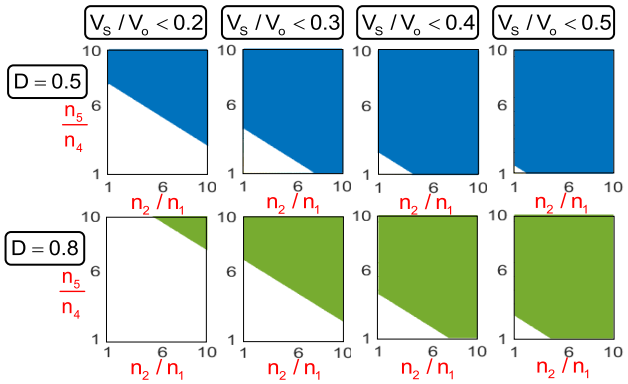

Fig. 8. Desired operation area for low switch voltage stress with respect to $(n_2 + n_3)/n_1$ and n_5/n_4 for different D values.

normalized form of the voltage stress (V_S/V_o) is with respect to D, a, $(n_2 + n_3)/n_1$, and n_5/n_4

$$V_S = \frac{V_i}{(1-D)^2}. \tag{10}$$

According to (10), the voltage stress of the power switch is not dependent on the CIs' turns ratio. Hence, by choosing low-voltage-rated power switches that feature low drain-to-source resistance as the power switch (S), both conduction loss reduction and high-voltage gain with high $(n_2+n_3)/n_1$ and n_5/n_4 values are achievable. The desired operation region from the switch voltage stress viewpoint for design consideration is shown in Figs. 7 and 8 where the higher "a" value, the lower the normalized switch voltage stress, the most common duty cycle range in high step-up converters ($0.5 < D < 0.85$) has low switch voltage stress, and the proposed structure for the converter presents an acceptably large switch design area. According to the following equations, the voltage stresses of the diodes can be calculated:

$$|V_{D1}| = \frac{V_i}{(1-D)}, \quad |V_{D2}| = \frac{V_i D}{(1-D)^2} \tag{11}$$

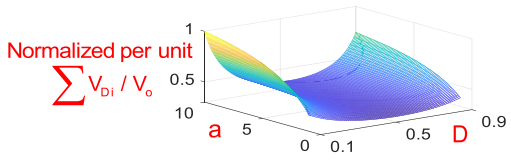

Fig. 9. Normalized per unit accumulative diodes voltage stress.

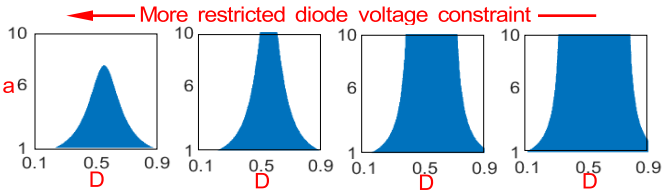

Fig. 10. Desired operation area for diodes' low accumulative voltage stress with respect to a and D.

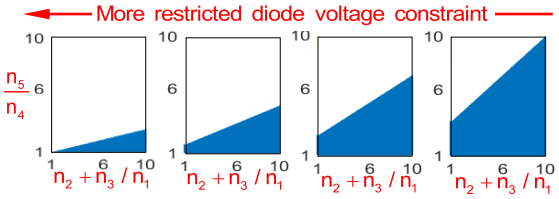

Fig. 11. Desired operation area for diodes' low accumulative voltage stress in $D = 0.5$ with respect to $(n_2 + n_3)/n_1$ and n_5/n_4.

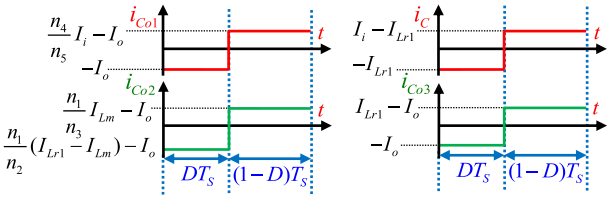

Fig. 12. Waveforms of the capacitors' current according to average value of inductors' current.

$$|V_{D3}| = \frac{V_i}{(1-D)}\left(\frac{n_5}{n_4}\right), \quad |V_{D4}| = \frac{V_i D}{(1-D)^2}\left(\frac{n_2+n_3}{n_1}\right) \tag{12}$$

$$|V_{D5}| = \frac{V_i}{(1-D)}\left(\frac{n_2+n_3}{n_1}\right), \quad |V_{D6}| = \frac{V_i}{(1-D)^2}. \tag{13}$$

Fig. 9 shows a 3-D view of the normalized per unit accumulative voltage stress on diodes to achieve the desired design region for the diodes' voltage in Figs. 10 and 11. According to these figures, the proposed converter provides an acceptable design area from both "a" and "D" viewpoints. A higher portion of the solution area is allocated to $0.5 < D$, which is more probable in the case of high step-up converters. In addition, increasing $(n_2 + n_3)/n_1$ is a better solution than n_5/n_4 to reach high-voltage gain by considering the diodes voltage stresses.

D. Current Stress Analysis

Fig. 12 shows the steady-state waveforms of i_C, i_{Co1}, i_{Co2}, and i_{Co3}, which are derived according to the inductors' average

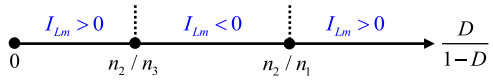

Fig. 13. Identification of magnetizing current sign.

currents, based on which and through the ampere-second balancing law (ASBL) on the capacitors, the average values of L_{r1} and L_m are obtained as follows:

$$I_{Lr1} = \frac{I_o}{(1-D)} \tag{14}$$

$$I_{Lm} = \frac{n_2 n_3 (1-D) - n_1 n_3 D}{n_1 n_2 (1-D)^2 - n_1 n_3 D(1-D)} I_o \tag{15}$$

where I_o is the output current equal to V_o/R and R is the output load. Based on (15), I_{Lm} can be either + or – according to the values of D, n_1, n_2, and n_3 (see Fig. 13). In Fig. 13, n_2/n_1 is assumed to be greater than n_2/n_3, considering the converter operating in the high step-up performance mode. Thus, according to (14) and (15) and considering the path of the current flow (shown in Fig. 2), the current stress of the power switch (S) is obtained as follows:

$$I_S = I_{Lr1} + I_i \tag{16}$$

Likewise, the current stresses of the diodes (D_1–D_6) in their conducting mode are calculated as follows:

$$I_{D1} = I_{D2} = I_i, \quad I_{D3} = (n_4/n_5) I_i \tag{17}$$

$$I_{D4} = (n_1/n_2)(I_{Lr1} - I_{Lm}), \quad I_{D5} = (n_1/n_3) I_{Lm}, \quad I_{D6} = I_{Lr1}. \tag{18}$$

E. Alleviation in Output Voltage Ripple

Even though the voltages in the output ports are regulated with an identical degree of freedom (D), V_{o1}, V_{o2}, and V_{o3} do not interact with each other regulation. Hence, the proposed triple-output port converter can be adjusted in an optimal operation zone by setting D, n_2/n_1, and n_3/n_1 to alleviate the amount of the overall output voltage ripple (v_o). Employing the current waveforms in Fig. 12, the schematic of the voltage ripple from each port (v_{o1}, v_{o2}, and v_{o3}) is shown in Fig. 14. Considering Fig. 12 and $dv_C/dt = i_C/C$, it can be inferred that dv_{o1}/dt and dv_{o3}/dt are negative and positive in DT_S and $(1-D)T_S$, respectively. Nevertheless, charging or discharging state of V_{o2} is conditional on the values of D, n_2/n_1, and n_3/n_1. Hence, the reverse sign of dv_{o2}/dt compared to dv_{o1}/dt and dv_{o3}/dt results in the reduced v_o by $|v_{o1}+v_{o3}-v_{o2}|$. In Fig. 14(a) and (b), the slopes of $V_{o1}(V_{o3})$ and V_{o2} have identical and different signs, respectively. Subsequently, Fig. 14(b) shows a better condition. The output voltage can be reduced if the following condition is satisfied:

$$\frac{n_2(1-D) - n_1 D}{n_2(1-D)^2 - n_3 D(1-D)} < 1. \tag{19}$$

Accordingly, the operation zone of the alleviated v_o is shown in Figs. 15 and 16. The operation zone in Fig. 15 is demonstrated with respect to n_2/n_1 and n_3/n_1 with different values of D. As shown in Fig. 15, the colored area shows the alleviated v_o. One can see that the higher n_2/n_1 and n_3/n_1 in the desired region, the higher V_o, the lower v_o, and accordingly, considerably lower ratio of output voltage ripple to the output voltage (v_o/V_o) will result. Likewise, the intended zone is shown in Fig. 16 in terms of n_2/n_1 and D. This zone includes a considerable part of the likely operation zone. It is clear that the intended zone is wider with a higher D in Fig. 15 and larger n_3 to n_1 ratio, according to Fig. 16. The small output voltage ripple feature of the proposed structure makes the converter an interesting option for some industrial applications such as electroplating.

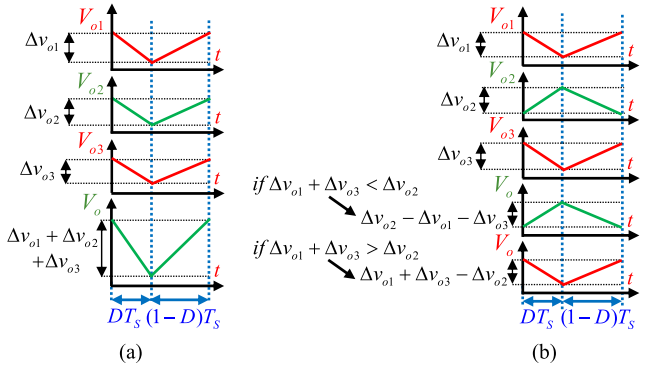

Fig. 14. Output voltage ripple. (a) Additional. (b) Subtractive (desired).

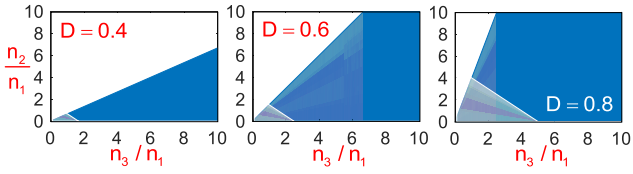

Fig. 15. Operation zone for the output voltage ripple alleviation according to n_2 to n_1 ratio and n_3 to n_1 ratio.

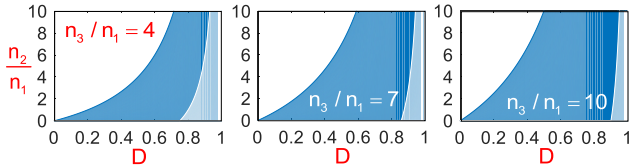

Fig. 16. Operation zone for the output voltage ripple alleviation in terms of n_2/n_1 and D.

F. Input Current Ripple

Considering the operational analytics presented in Section II-A, the normalized input current ripple is equal to

$$\frac{\Delta i_L}{I_i} = \frac{DR}{f_S L M^2}. \tag{20}$$

According to (20), the desired operation region for the input CI to reach a specific input current ripple is expressed in Fig. 17. In this figure, higher "D" and "a" correspond to lower normalized input current ripple, which leads to small CI size for a certain L, and accordingly, high power density.

G. Discontinuous Conduction Mode-CCM Boundary

According to (9) and the boundary conduction mode average input current ($I_{iB} = i_L/2$), the average output current and load

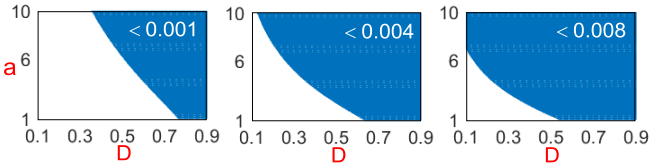

Fig. 17. Desired operation zone of input CI for different $i_L f_s L/RI_i$ limitations with respect to a and D.

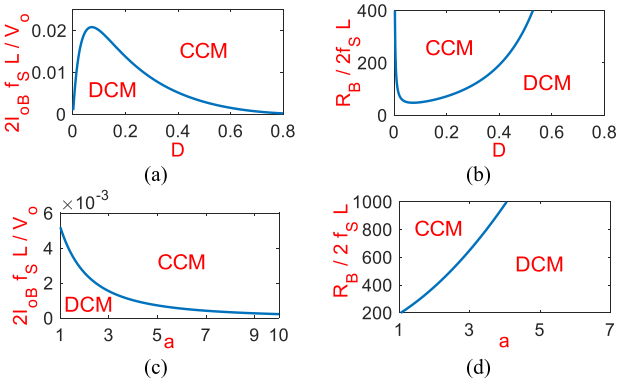

Fig. 18. BCM operational characteristics. (a) and (b) Normalized output current and normalized load resistance in $a = 3$. (c) and (d) Normalized output current and normalized load resistance in $D = 0.6$.

resistance in boundary conduction mode can be obtained as follows:

$$I_{oB} = \frac{DV_o}{2f_S LM^2}, \quad R_B = \frac{2f_S LM^2}{D}. \tag{21}$$

According to (21), the operation zone of CCM can be recognized on the normalized output current in Fig. 18(a) and (c). In addition, the operation zone in discontinuous conduction mode (DCM) is shown in load resistance planes in Fig. 18(b) and (d). According to Fig. 18, it can be inferred that increasing "a" yields a wider solution region in CCM for the normalized output current. As "a" becomes larger in DCM, the solution space widens for load resistance.

H. DCM Operation

Since the proposed converter structure utilizes two CIs, various DCM conditions can be introduced. As two mostly likely DCM conditions, discontinuous currents of only L_r and both L_k and L_r are considered in this article, which yields DCM and extremely DCM (EDCM), respectively. In Fig. 19, the voltages of the inductors in DCM and EDCM are demonstrated. According to Fig. 19 and the VSBL, the voltage gains in DCM and EDCM can be obtained as follows:

$$M_{\mathrm{DCM}} = \frac{\mathrm{D}_1}{\mathrm{D}_1+\mathrm{D}_2}\left(\frac{n_2 - n_2\mathrm{D}_1 + n_3\mathrm{D}_2}{n_1(1-\mathrm{D}_1)^2}\right) + \frac{n_5\mathrm{D}_1}{n_4\mathrm{D}_2} + \frac{1}{(1-\mathrm{D}_1)^2} \tag{22}$$

$$M_{\mathrm{EDCM}} = \frac{(1-\mathrm{D}_4)}{(\mathrm{D}_2+\mathrm{D}_3)}\left(\frac{\mathrm{D}_1}{n_1(\mathrm{D}_1+\mathrm{D}_2)}\left(n_2+\frac{n_3\mathrm{D}_2}{1-\mathrm{D}_1}\right)+\frac{1}{1-\mathrm{D}_1}\right) + \frac{n_5\mathrm{D}_1}{n_4\mathrm{D}_2}. \tag{23}$$

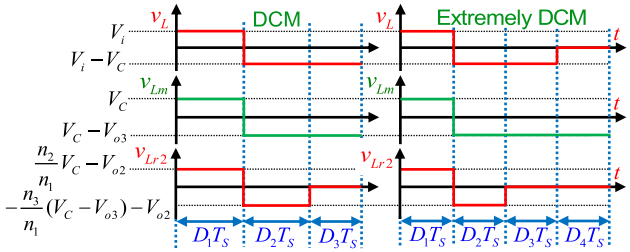

Fig. 19. Waveforms of inductors' voltage in two key discontinuous conduction operation modes.

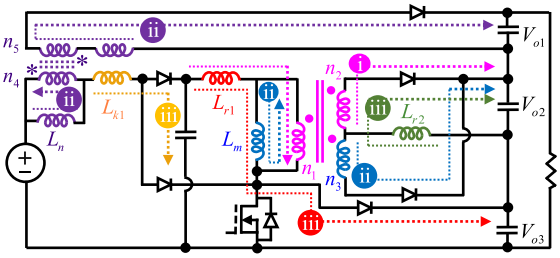

Fig. 20. Graphical paths of inductive power flow in the proposed converter solution.

I. Efficient Inductive Utilization

The recycling of the stored energy in the passive components of the circuit and transferring it to the load have been accomplished by utilizing various capacitive and inductive methods. These methods were meant to avoid the circulating current. The inductors' discharge paths to the output load are shown in Fig. 20. According to Fig. 20, the proposed converter structure provides a path to guide the stored energy of C to C_{o2} via n_1 and n_2 utilizing a forward method during DT_S, saves the stored magnetizing energy of L_n and L_m to C_{o1} and C_{o2}, respectively, utilizing a flyback method during $(1-D)T_S$, and reprocesses the harvested energy of L_{k1}, L_{r2}, and L_{r1} toward C, C_{o2}, and C_{o3}, respectively. Note that these energy flow paths correspond to their numbers in Fig. 20. Since the energy of all parasitic inductances (including leakage and magnetizing) is recycled, there is no need for an accurate design feature for the CIs to realize the intended operation. Hence, a basic and simple CI can also be employed in the proposed structure.

J. Energy Analysis

Using the following equations, the exchanged energy of each passive element during one switching period $(1/f_s)$ can be calculated:

$$\Delta w_L = \frac{M^2V_i^2D}{Rf_S}, \quad \Delta w_{Lr} = \frac{\mathrm{DMV}_i^2(n_2 - D(n_2+n_3))}{n_1Rf_S(1-D)^2} \tag{24}$$

$$\Delta w_{Lm} = \frac{MV_i^2D(n_2n_3(1-D) - n_1n_3D)}{Rf_S(n_1n_2(1-D)^3 - n_1n_3D(1-D)^2)} \tag{25}$$

$$\Delta w_{Co1} = \frac{MV_i^2D^2n_5}{Rf_S(1-D)n_4}, \quad \Delta w_{Co3} = \Delta w_{\mathrm{C}} = \frac{MV_i^2D}{Rf_S(1-D)^2} \tag{26}$$

$$\Delta w_{Co2} = \frac{MV_i^2D(n_2+n_3)}{Rf_Sn_1(1-D)}\left(\frac{n_2(1-D)-n_1D}{n_2(1-D)-n_3D} - 1 + D\right). \tag{27}$$

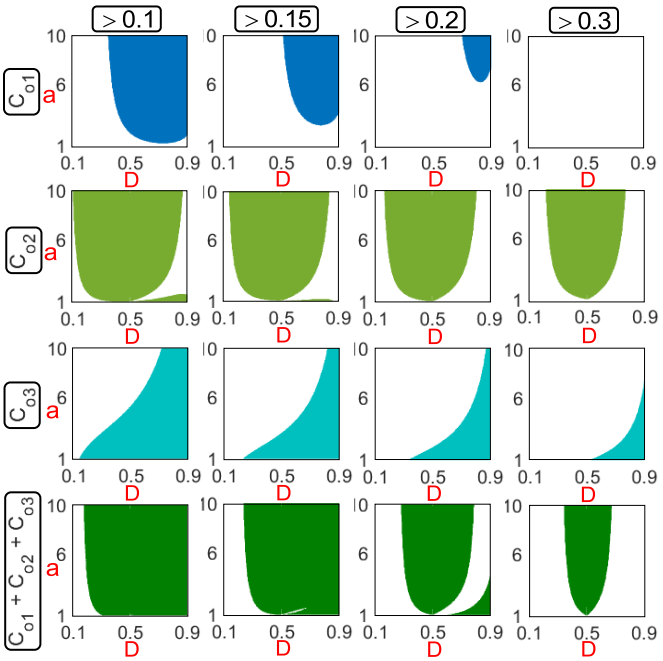

Fig. 21. Desired operation region for high energy transfer of output capacitors with different $w_C f_s R/V_o^2$ limitations.

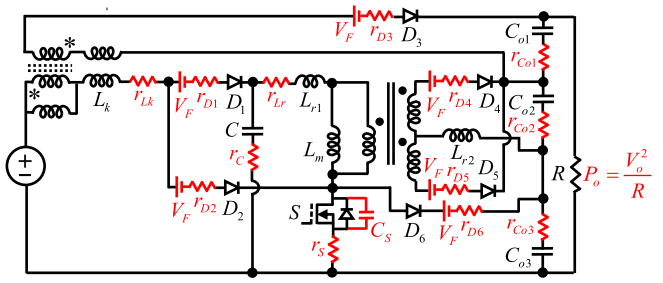

Fig. 22. Real (nonideal) model of the components of the proposed converter.

Equations (26) and (27) lead to Fig. 21, which demonstrates the desired operation region of the proposed converter to obtain high energy transfer in the output capacitors with different $w_C f_s R/V_o^2$ limitations. This figure presents the energy characteristics of the output capacitors in each row, which results in the overall feature in the last row. Moreover, the limitation becomes more restricted from left to right. According to Fig. 21, C_{o1} and C_{o2} transfer the lowest and the highest energy in the same operational condition, $0.5 < D$, and higher "a" have higher energy transfer, and the proposed converter presents high energy transfer (power density) in most of its common operation region at the output terminal.

III. Power Loss Assessment

The model, which is shown in Fig. 22, demonstrates the components of the proposed converter, including their real circuit representations. In this practical model, internal resistance is considered in series with the passive components, the diodes are represented with their forward voltage drop (V_F) and series resistance (r_D), and a drain-to-source on resistance (r_S) models the conduction loss, and also, a parasitic capacitance (C_S) model indicates the switching losses of the switch S. Besides,

TABLE I
Power Loss Equations of Components

Component	Power Loss Equation
S (Conduction Loss)	$P_S^{Cond}=\frac{r_S P_o D}{R}\left(\frac{1}{1-D}+M\right)^2$
S (Switching Loss)	$P_S^{Sw}=\frac{f_S C_S P_o R}{2M^2(1-D)^4}$
D_1	$P_{D1}=\frac{r_{D1}P_o M^2(1-D)}{R}+V_F M(1-D)\sqrt{\frac{P_o}{R}}$
D_2	$P_{D2}=\frac{r_{D2}P_o M^2 D}{R}+V_F MD\sqrt{\frac{P_o}{R}}$
D_3	$P_{D3}=\frac{r_{D3}n_4^2 P_o M^2(1-D)}{n_5^2 R}+V_F M(1-D)\frac{n_4}{n_5}\sqrt{\frac{P_o}{R}}$
D_4	$P_{D4}=\frac{r_{D4}Dn_1^2}{n_2^2}(I_{Lr1}-I_{Lm})^2+\frac{V_F Dn_1}{n_2}(I_{Lr1}-I_{Lm})$
D_5	$P_{D5}=\frac{r_{D5}n_1^2 I_{Lm}^2(1-D)}{n_3^2}+\frac{V_F I_{Lm}n_1(1-D)}{n_2}$
D_6	$P_{D6}=\frac{r_{D6}P_o}{R(1-D)}+V_F\sqrt{\frac{P_o}{R}}$
L_k and L_{r1} (Winding Loss)	$P_{Lk}^W=\frac{r_{Lk}M^2P_o}{R}$, $P_{Lr1}^W=\frac{r_{Lr}P_o}{R(1-D)^2}$
CI_1 Hysteresis Loss	$P_{CI1}^{Hys}=\frac{C_{Hys}V_i^2D^2U_{CI1}}{4(1-D)^2n_1^2f_S A_{CI1}^2}$
CI_2 Hysteresis Loss	$P_{CI2}^{Hys}=\frac{C_{Hys}V_i^2D^2U_{CI2}}{4N^2f_S A_{CI2}^2}$
CIs Eddy Current Loss	$P_{CI1}^{Eddy}=\frac{C_{Eddy}V_i^2DU_{CI1}}{N^2A_{CI1}^2(1-D)^3}$, $P_{CI2}^{Eddy}=\frac{C_{Eddy}V_i^2DU_{CI2}}{N^2A_{CI2}^2(1-D)}$,
C	$P_C=\frac{r_C P_o}{R}\left(\frac{D}{(1-D)^2}+(1-D)(M-\frac{1}{1-D})^2\right)$
C_{o1}	$P_{Co1}=\frac{r_{Co1}P_o(1-D)}{RD}\left(\frac{n_2(1-D)-n_1D}{n_2(1-D)^2-n_3D(1-D)}-1\right)^2$
C_{o2}	$P_{Co2}=\frac{r_{Co2}P_o D}{R(1-D)}$

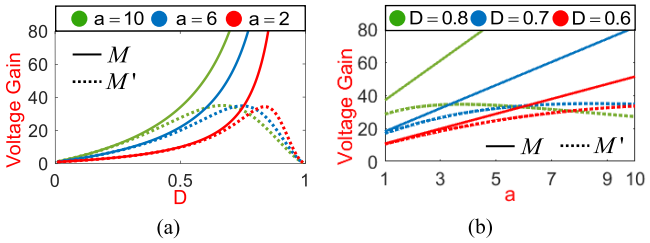

Fig. 23. Ideal and nondeal voltage gain comparison with respect to (a) duty cycle NS (b) CI turns ratio.

the coefficients of hysteresis and eddy current loss (C_{Hys} and C_{Eddy}), core effective cross-sectional area (A_{CI1} and A_{CI2}) of the CIs, and effective core volume (U_{CI1} and U_{CI2}) of the CIs are the empiric parameters in calculating the value of the core loss [22]. As stated by the steady-state analysis, the power loss equations of the components are summarized in Table I.

IV. Nonideal Converter Voltage Gain

According to the ideal converter voltage gain in (9) and the power loss calculations in Section III, the voltage gain of the converter in nonideal condition (M') can be obtained as

TABLE II

GENERAL COMPARISON OF THE PROPOSED CONVERTER WITH OTHER NEWLY INTRODUCED CONVERTERS BASED ON CIS. (**Pro:** PROPOSED)

Ref.	**Pro**	**[10]**	**[11]**	**[12]**	**[13]**	**[14]**	**[15]**	**[16]**	**[17]**
#S	1	1	2	4	2	2	2	6	2
#D	6	4	2	4	4	4	4	4	2
#L+CI	0+2	0+1	1+1	2+1	0+2	0+1	0+1	0+3	0+1
#C	4	4	4	3	3	5	5	7	5
#VMC	×	✓	✓	×	✓	✓	✓	✓	×
Ref.	**[18]**	**[19]**	**[20]**	**[23]**	**[24]**	**[26]**	**[27]**	**[30]**	**[31]**
#S	4	4	2	1	1	4	2	1	1
#D	6	2	6	4	4	0	2	4	5
#L+CI	2+2	0+2	0+2	0+1	0+1	0+1	1+1	0+1	0+1
#C	9	3	5	4	4	3	4	4	5
#VMC	✓	✓	✓	✓	✓	✓	✓	✓	✓

follows:

$$M' = \frac{M}{1 + (P_{\text{Loss}}/P_o)} \tag{28}$$

where P_{Loss} is the total power loss. Fig. 23 shows a comparison of M and M' with respect to "D" and "a."

V. DESIGN PROCEDURE OF PASSIVE COMPONENTS

The design of the passive circuit elements of the proposed converter can be accomplished using the following equations:

$$L_n = \frac{DV_i}{f_S \Delta i_L} \tag{29}$$

$$L_m = \frac{DV_i}{f_S \Delta i_{Lm}(1-D)}, \quad L_{r2} = \frac{n_2 DV_i(n_2 - D(n_2+n_3))}{n_1^2 f_S \Delta i_{Lr1}(1-D)} \tag{30}$$

$$C = \frac{DV_o}{f_S R \Delta v_C (1-D)}, \quad C_{o1} = \frac{DV_o}{f_S R \Delta v_{Co1}} \tag{31}$$

$$C_{o2} = \frac{V_o}{R f_S \Delta v_{o2}} \left(\frac{n_2(1-D) - n_1 D}{n_2(1-D) - n_3 D} - 1 + D \right) \tag{32}$$

$$C_{o3} = \frac{DV_o}{f_S R \Delta v_{o3}}. \tag{33}$$

VI. COMPARISONS

The converter design cannot fulfill all goals and may have some weak points, as well as realizing the power points. In this section, a comparison is made in the design and performance metrics corresponding to the proposed approach against other step-up dc–dc structures, which are based on the CI and have recently been introduced. A numerical comparison is made available in Table II with respect to the number of components (#S, #D, #L/CI, and #C) and VMC utilization. According to Table II, topologies in [10], [23], [24], [30], and [31] and the proposed structure possess the least achievable number of switches. Less switch yields less number of gate drivers, which also reduces the cost. Besides, in the proposed structure, a reasonable number of semiconductors have been employed, considering the utilization of three output terminals to harvest all passive components' energy. The presented structures in [16], [18], and [20] have the highest number of passive elements, leading to higher weight and size of the converter. Meanwhile, the number of employed passive components is acceptable in the proposed converter considering its generated output voltage level. In addition, the proposed structure operates without any VMCs, which results in no capacitive inrush currents during the switching transitions of VMC. The performance of voltage and energy is compared in Fig. 24. According to Fig. 24(a) and (b), the proposed approach achieves the highest voltage gain in comparison with similar works with respect to the duty cycle and turn ratio of the CI as the main duty. From the inductive point of view, the value of normalized w_L in the proposed structure is the highest in Fig. 24(c) and (d). According to Fig. 24(c) and (d) and considering the fact that a normalized form has been chosen for comparison, it can be inferred that the proposed converter utilizes the lowest size inductor in its input in a certain V_i, i_L, and f_s, the amount of power density in the proposed dc–dc converter is the highest, and the proposed converter is applicable in renewable energy applications due to its features. In order to provide a comprehensive evaluation, a cost function (CF) is defined as

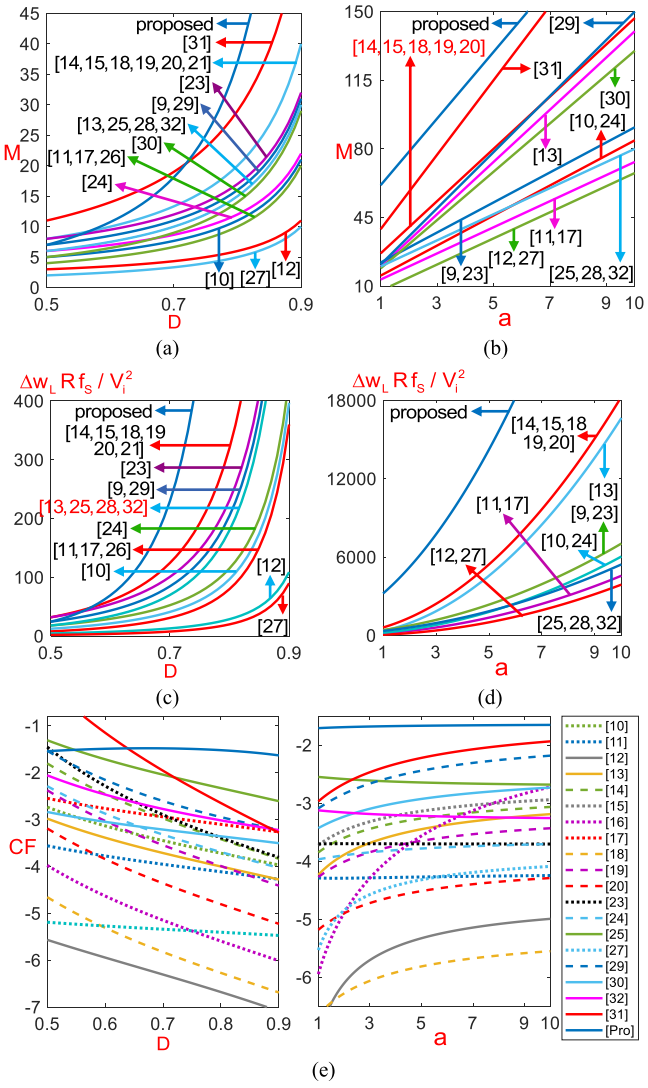

Fig. 24. Comparison of the CI-based dc–dc converters' performances in CI turn ratio of 1 and $D = 0.85$. (a) and (b) Output voltage gain. (c) and (d) Normalized transferred energy of the input CI in one switching cycle. (e) Generalized CF.

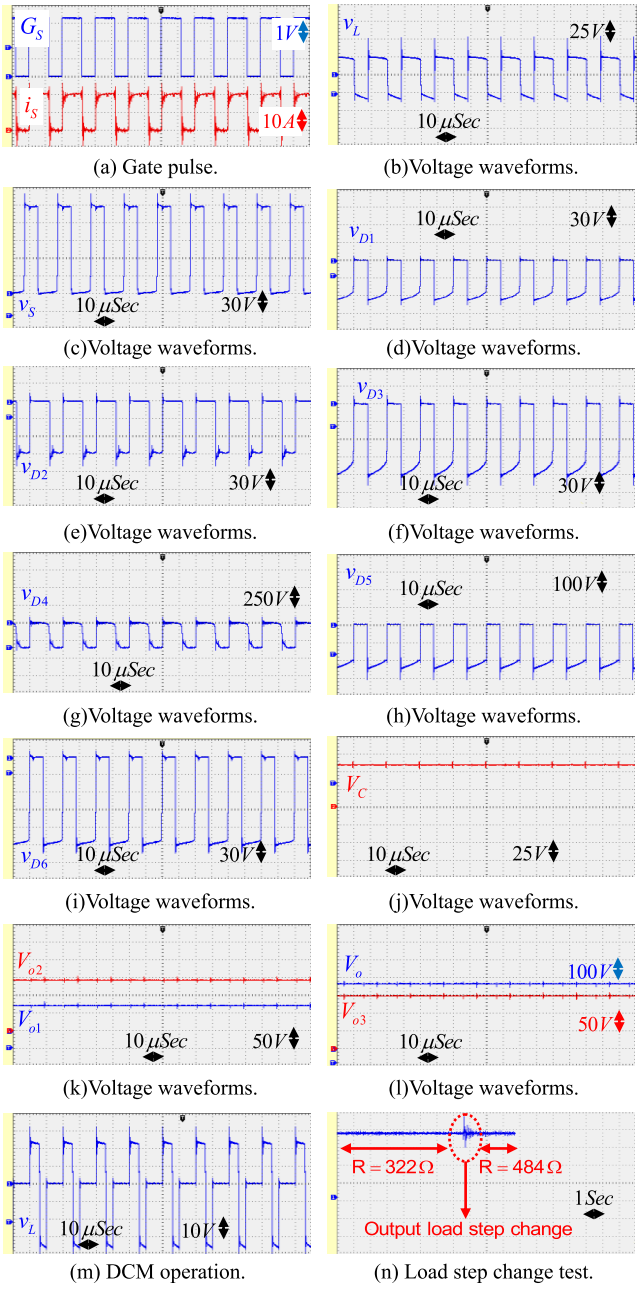

Fig. 25. Experimental results. (a) Gate pulse. (b)–(l) Voltage waveforms. (m) DCM operation. (n) Load step change test.

follows:

$$\mathrm{CF} = +x_1\hat{M} - x_2\Delta\hat{i}_L + x_3\Delta\hat{w}_L - x_4\sum\hat{V}_S - x_5\sum\hat{V}_D - x_6\hat{N}_S - x_7\hat{N}_D - x_8\hat{N}_L - x_9\hat{N}_C - x_{10}\hat{N}_{\mathrm{OM}} - x_{11}\mathrm{V\hat{M}C} \quad (34)$$

where $\hat{M}$, $\Delta\hat{i}_L$, $\Delta\hat{w}_L$, $\sum\hat{V}_S$, and $\sum\hat{V}_D$ are the normalized voltage gain, input current ripple, input energy, and accumulative switch and diode voltage stresses, respectively, $\hat{N}_S$, $\hat{N}_D$, $\hat{N}_L$, $\hat{N}_C$, and $\hat{N}_{\mathrm{OM}}$ are the normalized number of utilized switches, diodes, inductors, capacitors, and operational modes, respectively, in each converter. Note that, each aforementioned factor is normalized with the highest value of that parameter among converters, which leads them to the values of "≤ 1." Furthermore, $\mathrm{V\hat{M}C}$ is equal to "1" or "0" for the converters

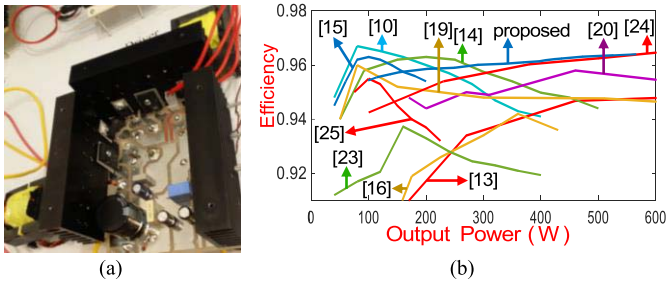

Fig. 26. (a) Prototype. (b) Converter efficiency with respect to the output power.

with or without VMCs, and x_i are the weight coefficients that are assumed as $x_i = 1$ in this article. In (34), the features and drawbacks are presented with "+" and "−" signs, respectively. According to the definitions, higher CF results in better converter characteristics from the generalized point of view, which is assessed in Fig. 24(e). Based on the highest CF value of the proposed converter in Fig. 24(e), it can be deduced that the proposed converter expresses notable promising advantages with an economical, high power density, ultrahigh-voltage gain, low-volume, uncomplicatedly-controlled, and efficient topology.

VII. Experimental Validation

A 600-W prototype with the power density of 1.028 W/cm^3 has been provided to validate the theoretical analytics of the proposed approach. For the circuit elements, IRFP4868pbf, HER3003PT, and HER3006PT are selected as the switch and diodes, respectively. One 33-μF, one 22-μF, and two 6.8-μF electrolyte capacitors are chosen for C, C_{o1}, C_{o2}, and C_{o3}, respectively, to limit the voltage ripple by 2% in V_C, V_{Co1}, V_{Co2}, and V_{Co3} based on (31) and (32). Moreover, $n_1 = 8$, $n_2 = 16$, $n_3 = 16$, $n_4 = 15$, and $n_5 = 30$ are designed for the CIs with EE55 cores. The control of the proposed converter is implemented by the LPC1768 ARM microcontroller.

In the experiment, the input voltage and power of the proposed converter are $V_i = 24$ V and $P_{\mathrm{in}} = 416$ W, respectively. In addition, the switching frequency is $f_s = 50$ kHz. The results of the test are shown in Fig. 25. According to Fig. 25(a), the applied gate pulse of the power switch S is $D = 0.6$, which results in the switch current curve with $I_S = 20$ A. In this duty cycle, v_L is shown in Fig. 25(b). v_L in the experimental results confirms the theoretical charge ($v_L \approx 24$ V) and discharge ($v_L \approx 36$ V) values in DT_S and $(1 - D)T_S$, respectively. The voltage waveforms of the semiconductors are shown in Fig. 25(c)–(i), where the approximate voltage stresses of $V_S \approx 150$ V, $V_{\mathrm{D1}} \approx 60$ V, $V_{\mathrm{D2}} \approx 90$ V, $V_{\mathrm{D3}} \approx 120$ V, $V_{\mathrm{D4}} \approx 360$ V, $V_{\mathrm{D5}} \approx 240$ V, and $V_{\mathrm{D6}} \approx 150$ V are observed, validating (10)–(13), respectively. The proposed converter expresses low-voltage spikes during the switching transitions. Hence, the proposed structure is a good choice in the applications where high voltage and high frequency are required. Fig. 25(j)–(l) shows the voltages across C, C_{o1}, C_{o2}, and C_{o3}, where the experimental results of $V_C = 58$ V, $V_{Co1} = 70$ V, $V_{Co2} = 140$ V, and $V_{Co3} = 147$ V nearly realize $V_C = 60$ V, $V_{Co1} = 72$ V, $V_{Co2} = 144$ V, and $V_{Co3} = 150$ V as the theoretical results, respectively. As shown

in Fig. 15, the converter's operation point is located in the desired v_o reduction region that satisfies Fig. 14(b). The DCM is also applied to the prototype, and v_L is shown in Fig. 25(m), which validates the theoretical analytics in Fig. 19. Finally, the load step change effect on the output voltage is evaluated in Fig. 25(n), where the load value is increased. Eventually, the converter prototype and the efficiency plots comparison are shown in Fig. 26, which verifies the acceptable efficiency of the proposed topology.

VIII. Conclusion

A state-of-the-art high step-up dc–dc converter has been proposed in this study. The proposed structure has been analyzed and validated via a 600-W experimental prototype. It has several key characteristics, including employing different inductive and capacitive methods to transfer the input power and harvested magnetic energy to the output load, achieving a high-voltage gain with lower turns ratio in the CI, and utilizing a simple PWM control with an extensive duty cycle range. The major properties of the proposed approach were thoroughly investigated and numerically compared with those of the state-of-the-art architectures. The detailed design discussion is provided to achieve the desired operational region regarding the semiconductors' voltage stress reduction, power density improvement, and ripple reduction in the input current and output voltage to make them smoother. A 600-W prototype has also been provided to validate the theoretical analyses. The experimental results confirm the voltage gain of 14.8 and an appropriate efficiency range of 94.7%–95.8%.

References

[1] H. Tarzamni, E. Babaei, and A. Z. Gharehkoushan, "A full soft-switching ZVZCS flyback converter using an active auxiliary cell," *IEEE Trans. Ind. Electron.*, vol. 64, no. 2, pp. 1123–1129, Feb. 2017.

[2] H. Tarzamni, F. P. Esmaeelnia, M. Fotuhi-Firuzabad, F. Tahami, S. Tohidi, and P. Dehghanian, "Comprehensive analytics for reliability evaluation of conventional isolated multiswitch PWM DC–DC converters," *IEEE Trans. Power Electron.*, vol. 35, no. 5, pp. 5254–5266, May 2020.

[3] Y. Azadeh, E. Babaei, H. Tarzamni, and M. Sabahi, "Single-inductor dual-output DC–DC converter with capability of feeding a constant power load in open-loop manner," *IEEE Trans. Ind. Electron.*, vol. 66, no. 9, pp. 6906–6915, Sep. 2019.

[4] F. A. A. Meinagh, E. Babaei, H. Tarzamni, and P. Kolahian, "Isolated high step-up switched-boost DC/DC converter with modified control method," *IET Power Electron.*, vol. 12, no. 14, pp. 3635–3645, Nov. 2019.

[5] P. Kolahian, H. Tarzamni, A. Nikafrooz, and M. Hamzeh, "Multiport DC–DC converter for bipolar medium voltage DC micro-grid applications," *IET Power Electron.*, vol. 12, no. 7, pp. 1841–1849, Jun. 2019.

[6] H. Tarzamni, E. Babaei, F. P. Esmaeelnia, P. Dehghanian, S. Tohidi, and M. B. B. Sharifian, "Analysis and reliability evaluation of a high step-up soft switching push-pull DC–DC converter," *IEEE Trans. Rel.*, vol. 69, no. 4, pp. 1376–1386, Dec. 2020.

[7] S. H. Hosseini, A. Z. Gharehkoushan, and H. Tarzamni, "A multilevel boost converter based on a switched-capacitor structure," in *Proc. 10th Int. Conf. Elect. Electron. Eng. (ELECO)*, 2017, pp. 249–253.

[8] H. Trazamni, E. Babaei, and M. Sabahi, "Full soft-switching high step-up DC–DC converter based on active resonant cell," *IET Power Electron.*, vol. 10, no. 13, pp. 1729–1739, Oct. 2017.

[9] Y.-P. Hsieh, J.-F. Chen, T.-J. Liang, and L.-S. Yang, "Analysis and implementation of a novel single-switch high step-up DC–DC converter," *IET Power Electron.*, vol. 5, no. 1, pp. 11–21, Jan. 2012.

[10] Y.-P. Hsieh, J.-F. Chen, T.-J. Liang, and L.-S. Yang, "A novel high step-up DC–DC converter for a microgrid system," *IEEE Trans. Power Electron.*, vol. 26, no. 4, pp. 1127–1136, Apr. 2011.

[11] K.-B. Park, G.-W. Moon, and M.-J. Youn, "Nonisolated high step-up stacked converter based on boost-integrated isolated converter," *IEEE Trans. Power Electron.*, vol. 26, no. 2, pp. 577–587, Feb. 2011.

[12] W. Li, W. Li, X. He, D. Xu, and B. Wu, "General derivation law of non-isolated high-step-up interleaved converters with built-in transformer," *IEEE Trans. Ind. Electron.*, vol. 59, no. 3, pp. 1650–1661, Mar. 2012.

[13] W. Li, Y. Zhao, Y. Deng, and X. He, "Interleaved converter with voltage multiplier cell for high step-up and high-efficiency conversion," *IEEE Trans. Power Electron.*, vol. 25, no. 9, pp. 2397–2408, Sep. 2010.

[14] Y. Zhao, X. Xiang, C. Li, Y. Gu, W. Li, and X. He, "Single-phase high step-up converter with improved multiplier cell suitable for half-bridge-based PV inverter system," *IEEE Trans. Power Electron.*, vol. 29, no. 6, pp. 2807–2816, Jun. 2014.

[15] N. Molavi, E. Adib, and H. Farzanehfard, "Soft-switched non-isolated high step-up DC–DC converter with reduced voltage stress," *IET Power Electron.*, vol. 9, no. 8, pp. 1711–1718, Jun. 2016.

[16] Y. Hu, W. Xiao, W. Li, and X. He, "Three-phase interleaved high-step-up converter with coupled-inductor-based voltage quadrupler," *IET Power Electron.*, vol. 7, no. 7, pp. 1841–1849, Jul. 2014.

[17] H.-W. Seong, H.-S. Kim, K.-B. Park, G.-W. Moon, and M.-J. Youn, "High step-up DC–DC converters using zero-voltage switching boost integration technique and light-load frequency modulation control," *IEEE Trans. Power Electron.*, vol. 27, no. 3, pp. 1383–1400, Mar. 2012.

[18] L. He, X. Xu, J. Chen, J. Sun, D. Guo, and T. Zeng, "A plug-play active resonant soft switching for current-auto-balance interleaved high step-up DC/DC converter," *IEEE Trans. Power Electron.*, vol. 34, no. 8, pp. 7603–7616, Aug. 2019.

[19] M. Forouzesh, Y. Shen, K. Yari, Y. P. Siwakoti, and F. Blaabjerg, "High-efficiency high step-up DC–DC converter with dual coupled inductors for grid-connected photovoltaic systems," *IEEE Trans. Power Electron.*, vol. 33, no. 7, pp. 5967–5982, Jul. 2018.

[20] W. Li, Y. Zhao, J. Wu, and X. He, "Interleaved high step-up converter with winding-cross-coupled inductors and voltage multiplier cells," *IEEE Trans. Power Electron.*, vol. 27, no. 1, pp. 133–143, Jan. 2012.

[21] T. Liu, M. Lin, and J. Ai, "High step-up interleaved DC–DC converter with asymmetric voltage multiplier cell and coupled inductor," *IEEE J. Emerg. Sel. Topics Power Electron.*, vol. 8, no. 4, pp. 4209–4222, Jul. 2019.

[22] W. A. Roshen, "A practical, accurate and very general core loss model for nonsinusoidal waveforms," *IEEE Trans. Power Electron.*, vol. 22, no. 1, pp. 30–40, Jan. 2007.

[23] J. Ai and M. Lin, "High step-up DC–DC converter with low power device voltage stress for a distributed generation system," *IET Power Electron.*, vol. 11, no. 12, pp. 1955–1963, Oct. 2018.

[24] K.-C. Tseng, J.-T. Lin, and C.-C. Huang, "High step-up converter with three-winding coupled inductor for fuel cell energy source applications," *IEEE Trans. Power Electron.*, vol. 30, no. 2, pp. 574–581, Feb. 2015.

[25] H. Ardi, A. Ajami, and M. Sabahi, "A novel high step-up DC–DC converter with continuous input current integrating coupled inductor for renewable energy applications," *IEEE Trans. Ind. Electron.*, vol. 65, no. 2, pp. 1306–1315, Feb. 2018.

[26] H. Liu, L. Wang, Y. Ji, and F. Li, "A novel reversal coupled inductor high-conversion-ratio bidirectional DC–DC converter," *IEEE Trans. Power Electron.*, vol. 33, no. 6, pp. 4968–4979, Jun. 2018.

[27] A. Kumar and P. Sensarma, "Ripple-free input current high voltage gain DC–DC converters with coupled inductors," *IEEE Trans. Power Electron.*, vol. 34, no. 4, pp. 3418–3428, Apr. 2019.

[28] G. Wu, X. Ruan, and Z. Ye, "High step-up DC–DC converter based on switched capacitor and coupled inductor," *IEEE Trans. Ind. Electron.*, vol. 65, no. 7, pp. 5572–5579, Jul. 2018.

[29] Y. P. Siwakoti and F. Blaabjerg, "Single switch nonisolated ultra-step-up DC–DC converter with an integrated coupled inductor for high boost applications," *IEEE Trans. Power Electron.*, vol. 32, no. 11, pp. 8544–8558, Nov. 2017.

[30] T.-J. Liang, S.-M. Chen, L.-S. Yang, J.-F. Chen, and A. Ioinovici, "Ultra-large gain step-up switched-capacitor DC–DC converter with coupled inductor for alternative sources of energy," *IEEE Trans. Circuits Syst. I, Reg. Papers*, vol. 59, no. 4, pp. 864–874, Apr. 2012.

[31] K.-C. Tseng, C.-C. Huang, and C.-A. Cheng, "A single-switch converter with high step-up gain and low diode voltage stress suitable for green power-source conversion," *IEEE J. Emerg. Sel. Topics Power Electron.*, vol. 4, no. 2, pp. 363–372, Jun. 2016.

[32] S. B. Santra, D. Chatterjee, Y. P. Siwakoti, and F. Blaabjerg, "Generalized switch current stress reduction technique for coupled-inductor-based single-switch high step-up boost converter," *IEEE J. Emerg. Sel. Topics Power Electron.*, vol. 9, no. 2, pp. 1863–1875, Apr. 2021.

Hadi Tarzamni (Student Member, IEEE) was born in Tabriz, Iran, in 1992. He received the B.Sc. and M.Sc. degrees (Hons.) in power electrical engineering from the Faculty of Electrical and Computer Engineering, University of Tabriz, Tabriz, in 2014 and 2016, respectively. He is currently pursuing the Ph.D. degree in power electronics engineering with the Department of Electrical Engineering, Sharif University of Technology, Tehran, Iran.

Since January 2021, he has been a Visiting Researcher at the Department of Electrical Engineering and Automation, Aalto University, Espoo, Finland. He has authored or coauthored more than 20 journal and conference papers. He also holds six patents in the area of power electronics. His research interests include power electronic converters analysis and design, dc–dc converters, soft-switching and resonant converters, and reliability analysis.

Mr. Tarzamni was a recipient of the Best Paper Award at the 10th International Power Electronics, Drive Systems and Technologies Conference (PEDSTC) in 2019.

Mehran Sabahi was born in Tabriz, Iran, in 1968. He received the B.S. degree in electronic engineering from the University of Tabriz, Tabriz, in 1991, the M.S. degree in electrical engineering from Tehran University, Tehran, Iran, in 1994, and the Ph.D. degree in electrical engineering from the University of Tabriz in 2009.

In 2009, he joined the Faculty of Electrical and Computer Engineering, University of Tabriz, where he has been a Professor since 2021. His current research interests include power electronic converters and renewable energy systems.

Saeed Rahimpour was born in Zanjan, Iran, in 1991. He received the B.S. degree in electrical engineering from Zanjan University, Zanjan, Iran, in 2014, and the M.S. degree in electrical engineering, power electronics, and electrical machines from Guilan University, Rasht, Iran, in 2017.

He is currently conducting research in the field of power electronics. His current research interests include grid-connected Inverters, reliability of power converters, energy routers, and multilevel converters.

Matti Lehtonen (Member, IEEE) received the M.S. and Licentiate degrees in electrical engineering from Aalto University, Espoo, Finland, in 1984 and 1989, respectively, and the D.Sc. degree from the Tampere University of Technology, Tampere, Finland, in 1992.

Since 1999, he has been with the School of Electrical Engineering, Aalto University, where he is currently a Professor of IT applications in power systems. His main research interests include earth fault problems, and harmonic-related issues and applications of information technology in distribution automation and distributed energy management.

Payman Dehghanian (Senior Member, IEEE) received the B.Sc. degree from the University of Tehran, Tehran, Iran, in 2009, the M.Sc. degree from the Sharif University of Technology, Tehran, in 2011, and the Ph.D. degree from Texas A&M University, College Station, TX, USA, in 2017, all in electrical engineering.

He is currently an Assistant Professor at the Department of Electrical and Computer Engineering, George Washington University, Washington, DC, USA. His research interests include electric power systems engineering, reliability and resiliency modeling and assessment, sensor-driven analytics in energy networks, power system protection and control, asset management, and smart electricity grid applications.

Dr. Dehghanian was a recipient of the 2013 IEEE Iran Section Best M.Sc. Thesis Award in Electrical Engineering, the 2014 and 2015 IEEE Region 5 Outstanding Professional Achievement Awards, and the 2015 IEEE-HKN Outstanding Young Professional Award.